SCIENTIFIC REPORTS

OPEN

One-dimensional porous nanofibers of Co_3O_4 on the carbon matrix from human hair with superior lithium ion storage performance

Yanli Tan, Qiuming Gao, Chunxiao Yang, Kai Yang, Weiqian Tian & Lihua Zhu

One-dimensional (1D) hierarchical porous nanofibers of Co_3O_4 possessing of (220) facets on the carbon matrix from human hair ($H2@Co_3O_4$) with 20–30 nm in width and 3–5 μm in length are prepared by a facile solvothermal and calcination approach. The well crystallized small Co_3O_4 particles with the diameter of about 8–12 nm were closely aggregated together in the nanofibers. Electrochemical analyses show that the first discharge capacity of $H2@Co_3O_4$ electrode is 1368 mAh g^{-1} at the current density of 0.1 A g^{-1} based on the total mass of composite. A high reversible capacity of 916 mAh g^{-1} was obtained over 100 cycles at 0.1 A g^{-1}, presenting a good cycling stability. When cycled at a high current density of 1 and 2 A g^{-1}, the specific capacity of 659 and 573 mAh g^{-1} could be still achieved, respectively, indicating a superior power capability.

The growing demand for developing sustainable and green-energy sources is at the top of the agenda for the whole world[1–4], because of the increasing concerns on population growth and industrialization worldwide. As an electrochemical energy storage device, rechargeable lithium ion battery (LIB) is attracting widespread attention with a view to its application in popular modern electronics and hybrid electric vehicles, owing to its high energy and power density, long cyclic life, environmental friendliness and safety[5–9]. While there are still some challenges in the design of LIB[5,10], for example high stable power density output without obvious loss of the energy density. Therefore, a variety of appealing strategies have been utilized to fabricate the electrode materials to meet the improvement of electrochemical properties of LIB.

Recently, mixed-valence spinel cobalt oxide (Co_3O_4) nanocrystals were paid considerable attention for use as anode material in LIB based on its excellent chemical and physical properties, such as high theoretical capacity (890 mAh g^{-1}), environmental benignity, good chemical/thermal stability, highly reactive facets, and safety during operation[11–14]. However, the application of Co_3O_4 in practical LIBs is seriously hindered by the low rate capability and poor cycling performance, which are mainly caused by its low electrical conductivity and large volume change during the charge–discharge cycling. Thus, fabrication of high performance cobalt oxide-based electrode materials with satisfactory high charge/discharge rates and energy conversion efficiency is still a great challenge. Various approaches have been attempted to solve the above mentioned problems and can be mainly divided into two categories. One of the most commonly used methods is to design hybrid nanocomposites. Until now, many kinds of carbon and Co_3O_4 composites have been applied in LIBs, *e.g.*, graphene@Co_3O_4[13,15–17], carbon nanotube (CNT)@Co_3O_4[18–20],

Key Laboratory of Bio-inspired Smart Interfacial Science and Technology of Ministry of Education, Beijing Key Laboratory of Bio-inspired Energy Materials and Devices, School of Chemistry and Environment, Beihang University, Beijing 100191, P. R. China. Correspondence and requests for materials should be addressed to Q.-M.G. (email: qmgao@buaa.edu.cn)
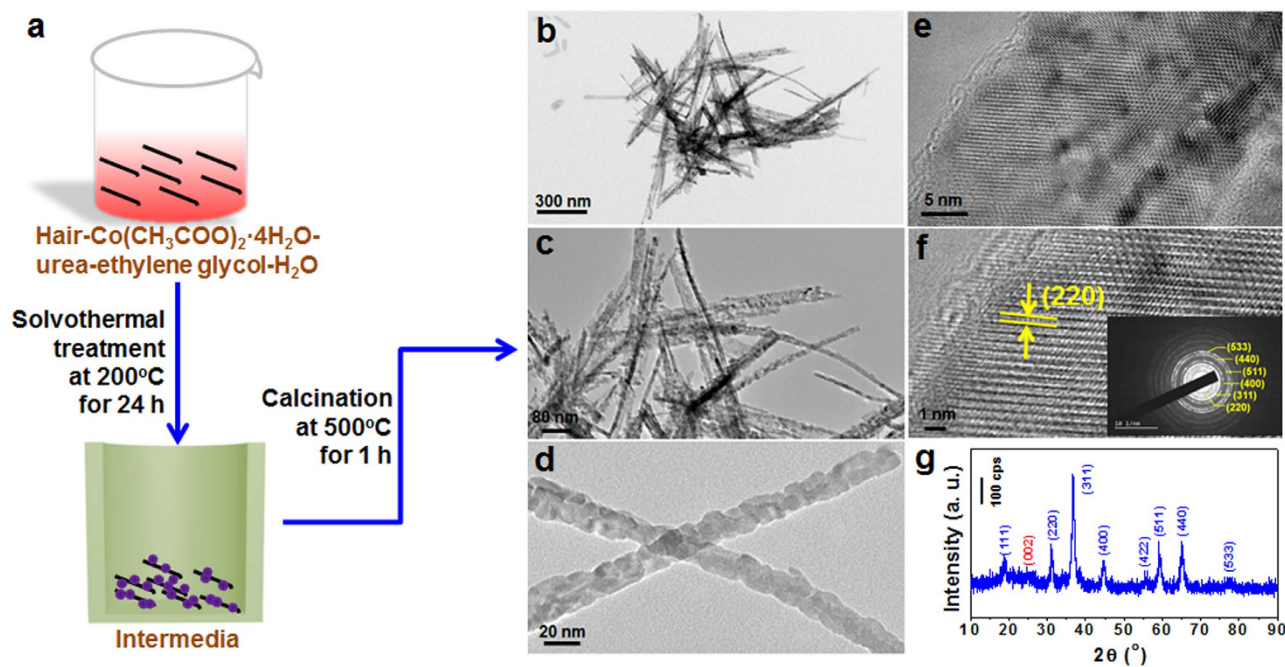
Figure 1. Formation process, morphology structure and phase analysis. a, A schematic of the synthesis steps for the H2@Co$_3$O$_4$ composite, which inlustrates the growth process of the sample. **b–d**, TEM images of the H2@Co$_3$O$_4$ composite, many 1D isolated nanobelts with 20–30 nm in width and 3–5 μm in length could be found. The small Co$_3$O$_4$ particles with the diameter of about 8–12 nm were closely aggregated together. **e–f**, HRTEM images of the H2@Co$_3$O$_4$ composite with the corresponding SAED patterns (inset of f), which show well crystallized nanostructure. And **g**, XRD patterns of the H2@Co$_3$O$_4$ composite.

carbon aeroge (CA)@Co$_3$O$_4$[21], onion-like carbon matrix@Co$_3$O$_4$[22], and monosaccharide-derived carbon@Co$_3$O$_4$[23]. All of them exhibit significantly improved performances as anodes compared to pure Co$_3$O$_4$, because the highly conductive carbonaceous matrix can increase the electrical conductivity, prevent the aggregation of active materials and cushion the drastic volume changes. The other strategy is to prepare nanometer-sized Co$_3$O$_4$ with designed textures and morphologies, for example, nanowires[24], nanosheets[11,25], peapod-like[10], nanotubes[26], octahedral cages[27], star-like[28], plate-like[29], microspheres[30], nanorods[31], nanobelts[32] and particles[19], which are believed to facilitate the electrolyte ion trapping and access to the designed nanometer-sized structures. In particular, one-dimensional (1D) hierarchical nanostructures have aroused much more interest in a variety of fields due to their rich accessible electro-active sites, fast Li$^+$ ion diffusion and potential synergetic properties or multi-functionalities[33–35]. Notably, the research revealed that crystal facet structure is important for lithium ion transport and distinctly affects the electrochemical properties of electrode materials[14,19,26,36,37]. Thus, the 1D hierarchical Co$_3$O$_4$ nanocrystal materials possessing of the exposed high energy facets will be highly pursued, since their electrochemical performance is believed to be greatly improved. Electrode materials with such ideal architecture can not only provide more active unites and multiple large contact areas, but also allow fast Li$^+$ ions transport between the electrolyte and electrode.

It is well known that the human hair is an easily obtained natural 1D polymer, which is mainly made up of entirely keratinized horny cells with the composition of ~51% carbon, 17% nitrogen, 21% oxygen, and so on[38]. In this paper, we report a facile approach of large-area growth for 1D hierarchical porous nanofibers of Co$_3$O$_4$ with (220) facets on the carbon matrix from human hair (denominated as H2@Co$_3$O$_4$) by solvothermal treatment of the mixture of hair-Co(CH$_3$COO)$_2$·4H$_2$O-urea-ethylene glycol-H$_2$O following with high-temperature calcination. The hair may serve as both the carbon precursor and the morphology guiding agent or "template" of the H2@Co$_3$O$_4$ composite nanofibers. The H2@Co$_3$O$_4$ nanofibers exhibit an excellent electrochemical energy stroage property as the LIB anode active material.

Results

A schematic of the growth process, morphology structures and phase analyses by the transmission electron microscopy (TEM), high resolution TEM (HRTEM), selective area electron diffraction (SAED) patterns and X-ray diffraction (XRD) patterns of the H2@Co$_3$O$_4$ composite are given in Fig. 1. First, the cleaned hairs were fully immersed in deionized water. Then, Co^{2+} ions were introduced into the above solution with a thorough mixing process, which enables a full adsorption of Co^{2+} ions on the surface

of hair substrate through charge attraction between the positively charged cobalt ions and the negtive charged functional groups of proteins in the hair. And then, a certain amount of urea was added into the mixture, resulting in the formation of cobalt oxide precursor. After solvothermal treatment and calcination, the composite of Co_3O_4 on the carbon matrix from human hair (named as H@Co_3O_4) was obtained (Fig. 1a).

The morphologies of the as-prepared H@Co_3O_4 composite could be controlled by modifying the calcination time of intermediate obtained from the solvothermal treatment. Three typical kinds of H@Co_3O_4 composites H1@Co_3O_4, H2@Co_3O_4 and H3@Co_3O_4 have been investigated which correspond to the different calcination time of the precursors (see Experimental Section for detail). As shown in Fig. 1b–d and S1-2, the H1@Co_3O_4, H2@Co_3O_4 and H3@Co_3O_4 composites present different morphologies with varied contents of carbon from 34.76, 10.78 down to 6.15 wt.% based on the thermogravimetric (TG) measurements (Fig. S4) via increasing calcination time from 0.5, 1 to 2 h at the temperature of 500 °C in air. The H1@Co_3O_4 composites were thin flake-like aggregates with several nanometers in thickness, 100–300 nm in width and 1–3 μm in length (Fig. S1). The draw ratio of about 10–50 is low due to the loosely aggregated Co_3O_4 particles with the diameter of about 5–10 nm anchored on the carbon matrix which is easily broken under the preparation condition. Many 1D isolated nanobelts with 20–30 nm in width and 3–5 μm in length could be found for the H2@Co_3O_4 composites (Fig. 1b,c). The draw ratio is about 100–500, which is about ten times of that of H1@Co_3O_4 composites. The small Co_3O_4 particles with the diameter of about 8–12 nm were closely aggregated together, indicating that there may be a good conductivity for the H2@Co_3O_4 composite material. When further prolonging the calcination time, there were hardly isolated nanobelts but the large bundles of H3@Co_3O_4 composite nanobelts could be clearly observed (Fig. S2), where the Co_3O_4 particles became a little larger than that of H1@Co_3O_4 and H2@Co_3O_4 composites. Without adding hair in the reaction system, the as-synthesized pure Co_3O_4 nanoparticles could be obtained, and the particles have an average diameter of about tens of nanometers (Fig. S3). Obviously, the diameter of the Co_3O_4 nanoparticles of H@Co_3O_4 composites is much smaller than that of pure Co_3O_4 material. Therefore, the addition of carbon substrate from hair fiber may reduce the particle size of the Co_3O_4 nanoparticles and change the aggregating degree of the particles so as to control the morphology of samples. Thus, the 1D isolated H2@Co_3O_4 composite nanobelts are expected to show markedly excellent electrochemical properties when used as the active material of LIB anode.

Some pores or vacancy defects may be found in the H2@Co_3O_4 nanobelts (Fig. 1d,e), which could be favorable for providing ideal charge pathway for transports of the electrons/lithium ions when used as the electrode material. TEM images in Fig. 1e and f show that H2@Co_3O_4 composite nanobelts possessed well crystallized nanostructure. The clear lattice spacing of 0.285 nm fringes agreeing well with the (220) lattice spacing of face-centered cubic (fcc) Co_3O_4[14] could be observed from Fig. 1f. The typical SAED patterns taken on the H2@Co_3O_4 composites (insert of Fig. 1f) can be indexed as (220), (311), (400), (511), (440) and (533) planes of the fcc Co_3O_4. The overall crystal structure and phase purity of the H2@Co_3O_4 composite were further identified by XRD patterns (Fig. 1g). The (111), (220), (311), (400), (422), (511), (440), and (533) peaks in the XRD patterns match well with that of the fcc Co_3O_4 (JCPDS No. 42-1467)[39], which is consistent with the HRTEM and SAED results. Moreover, the small broad diffraction peak appeared at 2θ around 25° indexed into the (002) reflection of the graphitic-type lattice (hexagonal, space group $P6_3/mmc$ (No. 194), and JCPDS card No. 65-6212) represents well-developed graphitization of the carbon matrix from the hair fibers, which may be helpful for the electron transmission along the aroma carbon layers, and the low intensity is owing to the small amount of carbon (10.78 wt.%) in the composite.

It is generally accepted that the hierarchical porosity of the material has a great influence on its performance in energy storage. The adsorption-desorption isotherms of nitrogen at 77 K were obtained to measure the specific surface area and pore size distribution (Fig. 2a) using the multiple-point Brunauer-Emmett-Teller (BET) method. The isotherm of the H2@Co_3O_4 composite is of typical type-IV with a desorption hysteresis at a pressure range of 0.7–1.0 P/P$_0$, according to the International Union of Pure and Applied Chemistry (IUPAC) classification, which suggests the presence of mesopores in the sample[40]. Moreover, when the relative pressure is close to 1, the amount of the adsorbed N_2 rapidly increases, indicating that macropores exist in the H2@Co_3O_4 composite. The nitrogen adsorption-desorption isotherms and pore size distribution of the H1@Co_3O_4, H3@Co_3O_4 and pure Co_3O_4 are shown in Figure S5 with the corresponding textural parameters listed in Table S1. The BET specific surface area of samples decreases with the increasing Co_3O_4 contents. However, the average pore diameter of the sample displays a slightly decreasing trend when the Co_3O_4 content increases due to the blocking of some meso- and/or macropores. The pore size distribution curve of H2@Co_3O_4 composite determined by the Barrette-Joynere-Halenda (BJH) method (insert in Fig. 2a) showed that the pore-size distribution is broad with the average pore size of around 3.73 nm. The hierarchical pore structure of the H2@Co_3O_4 composite may be helpful for its electrochemical performance, since the electrolyte can penetrate more sufficiently into the pores, thus leading to a higher electrolyte/electrode contact area and more facile intercalation for Li$^+$ ions in the electrolyte within the pores[41]. The BET specific surface area of the hierarchical H2@Co_3O_4 composite is calculated to be 42.33 m^2 g^{-1}. It is worth mentioning that the high BET specific surface area could be attributed to the porosities of the Co_3O_4 and carbon as well as to the formation of secondary pores between the Co_3O_4 and the carbon substrate. Such a pore structure can provide not only fast ionic transport channels but also sufficient buffer space for the volume
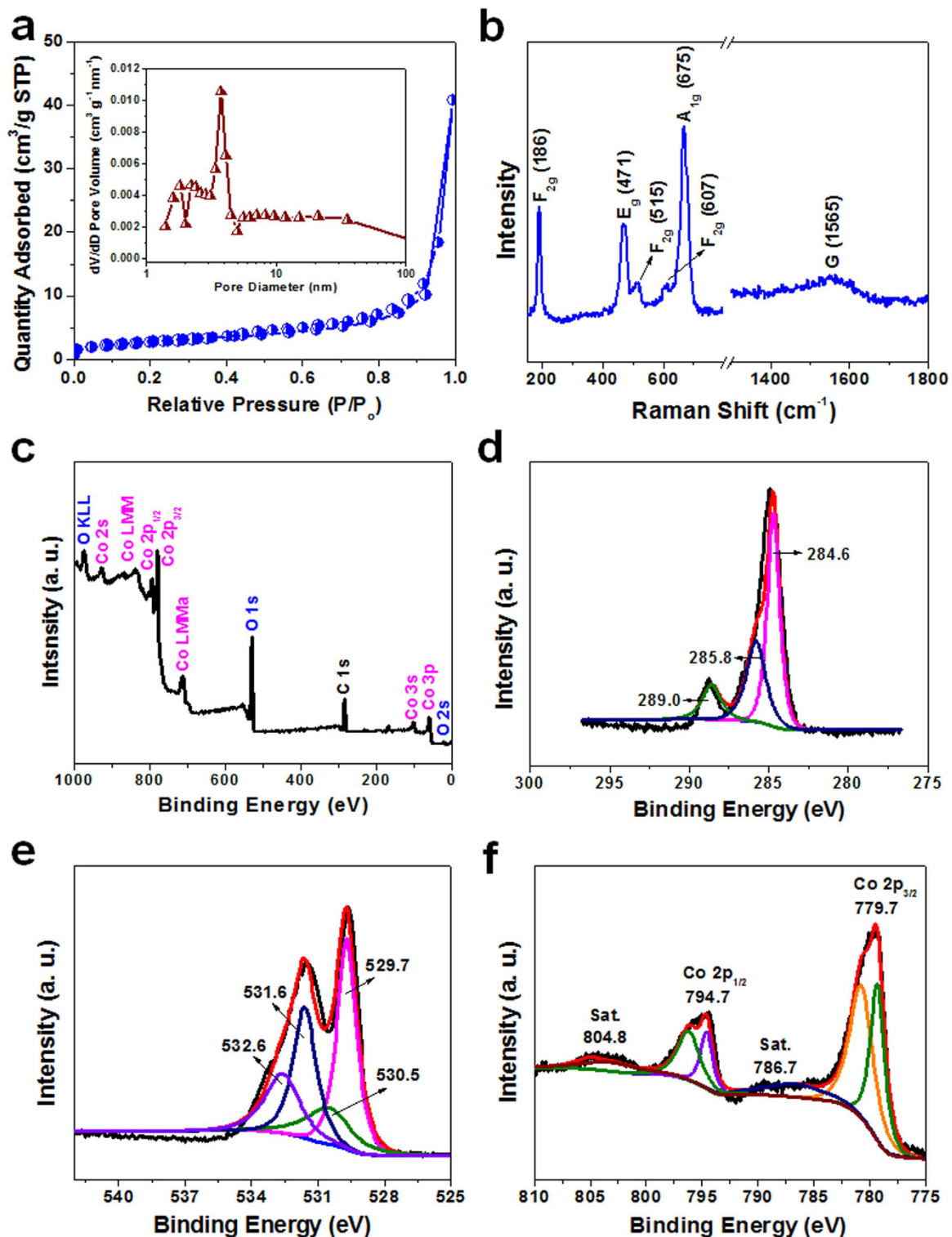
Figure 2. BET, Raman patterns and XPS tests. a, Nitrogen adsorption-desorption isotherms of the H2@ Co_3O_4 composite. Typical IV curves were obseved, indicating the mesoporous structure. The inset is pore size distribution, showing broad pore size distribution with the average pore size of 3.73 nm. **b**, Raman spectra of the H2@Co_3O_4. **c**, XPS survey spectrum of the H2@Co_3O_4, which indicates the existence of carbon, oxygen and cobalt elements. **d**, The high-resolution spectrum of the C 1s region, where the peak at 284.6, 285.8 and 289.0 eV is corresponding to nonoxygenated carbon atoms (C-C/C=C), carbon atoms in hydroxyl groups (C-OH/C-OCo) and carbon in carboxyl groups (HO-C=O), respectively. **e**, The high-resolution spectrum of the O 1s region, where the O 1s core level spectrum is broad and four Gaussians peaks were resolved. And **f**, The high-resolution XPS spectrum of the Co 2p, which shows two major peak with binding energy at 779.7 and 794.7 eV, corresponding to the Co $2p_{3/2}$ and Co $2p_{1/2}$ peak, respectively.

expansion of Co_3O_4[42]. Particularly at high current density, the high surface area and typical hierarchical pore structure may shorten the Li^+ ion diffusion path and reduce inner stress during Li^+ ion insertion/desertion processes in the LIB system, and further leads to large capacity, high rate performance and good cycling stability.

The $H2@Co_3O_4$ composite structure was further characterized by Raman spectroscopy. Three characteristic peaks (Fig. 2b) could be observed at 186, 515 and 607 cm^{-1}, which are corresponding to the F_{2g} mode of the crystalline Co_3O_4. The peak at 471 and 675 cm^{-1} can be attributed to the E_g and A_{1g} mode of Co_3O_4, respectively[43]. The phonon symmetries of the Raman peaks are caused by the lattice vibrations of the spinel structure, in which Co^{2+} and Co^{3+} cations are situated at tetrahedral and octahedral sites in the cubic lattice[44]. In addition, the G-band ($\sim$1565 cm^{-1}) corresponding to the sp^2-hybridy mode of the ordered graphitic carbon was observed for the sample[45]. There is no obvious disordered carbon D-band at $\sim$1350 cm^{-1}, indicating that the carbon substrate is lack of defects.

The surface information on the $H2@Co_3O_4$ sample was obtained by X-ray photoelectron spectroscopy (XPS). The binding energies obtained in the XPS spectra were calibrated using the C1s photoelectron peak at 284.8 eV as the reference. The sharp peak at 284.8, 531.1 and 780.7 eV (Fig. 2c) corresponds to the characteristic peak of C 1s, O 1s and Co 2p, respectively, indicating the existence of carbon, oxygen and cobalt elements. Figure 2d shows the high-resolution spectrum of the C 1s region. The peak at 284.6, 285.8 and 289.0 eV could be observed, corresponding to nonoxygenated carbon atoms (C-C/C=C), carbon atoms in hydroxyl groups (C-OH/C-OCo) and carbon in carboxyl groups (HO-C=O), respectively[46]. Figure 2e presents the high-resolution spectrum of O 1s. It can be seen that the O 1s core level spectrum is broad and four Gaussians peaks were resolved. The peak at the lower energy of 529.7 eV is associated with the lattice oxygen in the spinel Co_3O_4[47]. The other three peak at the higher energy of 530.5, 531.6 and 532.6 eV is associated with the oxygen in cobalt monoxide hydroxide ions, oxygen of the hydroxide ions and with the water adsorbed onto the surface of the Co_3O_4 nanoparticles, respectively[48]. The two forms of cobalt oxide, i.e., CoO and Co_3O_4, can be identified by different intensities of the shakeup satellites between the main peaks Co $2p_{3/2}$ and Co $2p_{1/2}$. Figure 2f exhibits the high resolution XPS spectrum of Co 2p, which shows two major peak with binding energy at 779.7 and 794.7 eV, corresponding to the Co $2p_{3/2}$ and Co $2p_{1/2}$ peak, respectively. The gap between the peaks is about 15 eV, which is a typical characteristic of the standard Co_3O_4 spectra[41]. In addition, the shake-up satellite peaks are at 804.8 and 786.7 eV, confirming the existence of Co^{2+} in the sample[32]. This result indicates that the composite is composed of Co_3O_4 and the oxygen bridges between Co_3O_4 and carbon in the $H2@Co_3O_4$ composite.

The unique structure motivates the $H2@Co_3O_4$ composite electrode with excellent lithium storage property, which was evaluated by using various electrochemical tests. Cyclic voltammetry (CV) was first conducted to investigate the electrochemical reaction process at a scan rate of 0.2 mV s^{-1} within the voltage window of 0.01–3.00 V (Fig. 3a). As to the first cathodic sweep, an irreversible peak appearing at 0.68 V was observed, which is attributed to the electrochemical reduction (lithiation) reaction of Co_3O_4 with Li^+ and the formation of solid electrolyte interphase (SEI) films[49]. For the anodic sweep, the oxidation peak at 1.40 and 2.17 V was recorded, corresponding to the decomposition of SEI film and the oxidation of the Co to Co_3O_4, respectively[27]. Compared to the discharge-charge voltage plateaus, the cathodic peak negatively shifted and the anodic peak positively shifted due to the polarization of the electrode in the first cycle[50]. The lithium storage mechanism of the electrode can be described by the electrochemical reaction of Li with Co_3O_4: $Co_3O_4 + 8Li = 4Li_2O + 3Co$. During the subsequent cycles, a decrease of the peak intensity and a shift of the potential in the positive direction were revealed compared to that of the first cycle, which indicate the occurrence of some irreversible processes in the electrode material in the initial cycle. From the second cycle, the CV curve of the sample showed two cathodic peak at 0.78 and 1.13 V, and the corresponding anodic peak was at 1.40 and 2.20 V, respectively. The pair of cathodic and anodic peaks possibly originated from the redox reaction of $Co^{3+/2+}/Co^0$[51]. Specifically, Co_3O_4 has a normal spinel structure with Co^{2+} and Co^{3+} ions in a cubic close packed lattice of oxide anions, so the redox reaction of $Co^{3+/2+}/Co^0$ is a complex multistep reaction behavior during the discharge processes[52]. Moreover, the two oxidation peaks hardly exhibited change in the subsequent cycles, which indicate a good reversibility and reproducibility of the electrochemical reaction for lithium ion storage. The CV behavior indicates that the overall capacity of $H2@Co_3O_4$ composite arises mainly from the properties of the metal oxide, which further shows that the excellent reversibility and stability of the electrode material have been gradually built after the initial cycle.

Typical charge/discharge curves of the $H2@Co_3O_4$ composite electrode were examined for the 1st, 2nd, 10th, 20th, 50th and 100th cycles based on the standard Co_3O_4/Li half-battery configuration at 0.1 A g^{-1} (Fig. 3b). In the first discharge curve, a long voltage plateau was shown at about 1.00 V vs Li^+/Li and the voltage dropped gradually until the end of the discharge. The following sloping region may be relative with the reversible Li-driven decomposition of Co_3O_4 as well as formation of the SEI film. The voltage slope should be associated with the irreversible reactions to form the SEI film and possibly interfacial lithium storage, which can lead to an extra reversible capacity[53,54]. Therefore, the actual reversible capacity of Co_3O_4 are usually larger than the theoretical value (890 mAh g^{-1})[12]. In the following cycles, the voltage capacity curves were highly consistent indicating superior cycle stability of the $H2@Co_3O_4$ nanofibers during the lithiation-delithiation processes.
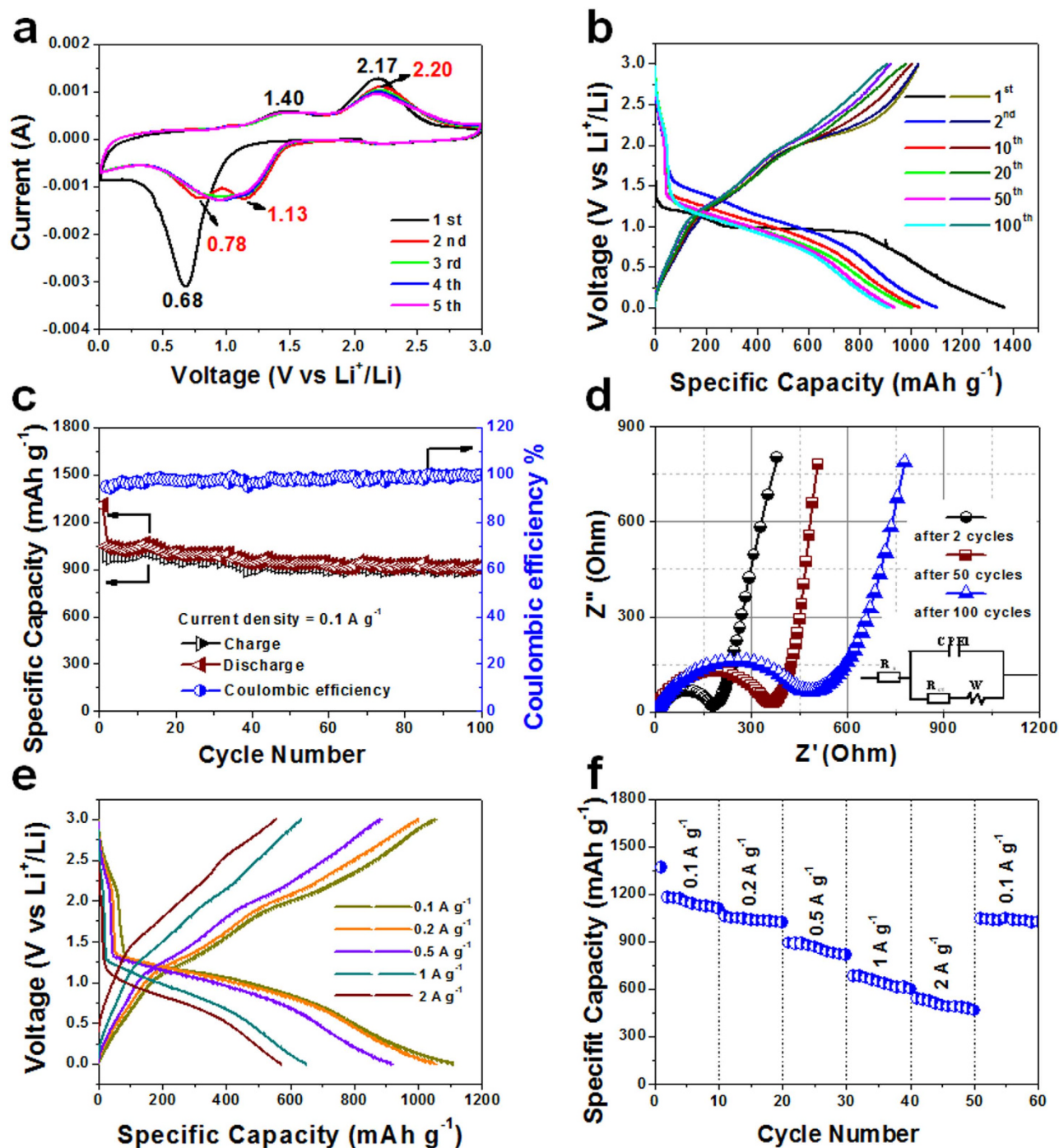
Figure 3. Electrochemical characterization of the H2@Co₃O₄ composite as anode for LIB applications. a, Representative CV curves at a scan rate of 0.2 mV s⁻¹. **b,** Galvanostatic charge/discharge profiles for the 1st, 2nd, 10th, 20th, 50th and 100th cycles at 0.1 A g⁻¹. **c,** Plots of charge–discharge capacities versus cycle number and Coulomb efficiency at a current density of 0.1 A g⁻¹ between 0.01 and 3.0 V. **d,** EIS curves after 2, 50 and 100 cycles with the inset of the simulation model of the equivalent circuit. **e,** Charge–discharge curves at different current rates. And **f,** Rate performance at various current densities from 0.1 to 2 A g⁻¹ in the voltage range of 0.01–3.0 V.

For comparison, we also measured the performance of H1@Co₃O₄ (Fig. S6a), H3@Co₃O₄ (Fig. S6b) and pure Co₃O₄ (Fig. S6c) prepared by the similar procedure with different calculation time under the same electrochemical conditions. The first discharge capacities of H1@Co₃O₄, H2@Co₃O₄, H3@Co₃O₄ and pure Co₃O₄ were successively 926, 1368, 1015, and 1195 mAh g⁻¹ based on the total mass of composites. From the second cycle, however, the H2@Co₃O₄ composite electrode presented

Material	Morphology	Current density [mA g^{-1}]	The first discharge/charge capacity [mAh g^{-1}]	Initial Coulombic efficiency [%]	Capacity [mAh g^{-1}] after (x) cycles	Ref.
Co$_3$O$_4$-graphene	nanosheet	143	1430/730	51.1	630 (50)	16
Co$_3$O$_4$/r-GO	nanowall	180	1236/707	57.2	673 (100)	15
Co$_3$O$_4$/C	nanoplate	100	1254/1035	82.5	1079 (50)	40
Co$_3$O$_4$/CNT	hollow	50	1420/977	68.8	977 (100)	20
G-Co$_3$O$_4$	microsphere	100	1533/1266	82.6	820 (35)	30
Co$_3$O$_4$@carbon	peapod-like	890	1800/1050	58.3	800 (50)	10
Co$_3$O$_4$/graphene	nanoparticle	58	1097/753	68.6	800 (30)	13
Co$_3$O$_4$-graphene	hexagonal ring	178	1029/750	72.9	748 (50)	17
H2@Co$_3$O$_4$	nanofiber	100	1368/1031	75.4	916 (100)	Our work

Table 1. The specific capacity of H2@Co$_3$O$_4$ nanofibers compared with the reported results on the Co$_3$O$_4$-based materials with different morphologies.

much better electrochemical lithium storage performance than the other three electrodes. Afterward, the following discharge curves tended to be stable with a value of 916 mAh g^{-1} after 100 cycles, implying that the electrochemical reactions were proceeding into the cyclable stages. The Coulombic efficiency rapidly raised from 75.4% in the first cycle to 98.3% in the 50th cycle and then remained at above 99.2% in the 100th cycle. As for the H1@Co$_3$O$_4$ and H3@Co$_3$O$_4$ electrodes, the discharge capacity dropped to 566 and 650 mAh g^{-1} after 100 cycles, only remaining 61.1% and 64.0% of the initial capacity, respectively (Fig. S6a and b). Compared to that of the H1@Co$_3$O$_4$ and H3@Co$_3$O$_4$ composite electrodes, the pure Co$_3$O$_4$ electrode showed a larger discharge capacity in the first cycle but suffered from fast reversible capacity fading, where 573 mAh g^{-1} was observed for the 50th cycle and lower capacity of 293 mAh g^{-1} was gotten for the 100th cycle (Fig. S6c). This result indicates that on one hand, there is a strong synergistic effect between Co$_3$O$_4$ nanoparticles and carbon from the hair fibers in the H@Co$_3$O$_4$ composites, which becomes much more apparent with cycling and plays a key role in the excellent cyclic performance of the composite; and on the other hand, it is important to note that the content of carbon from the hair substrate influences the morphology of the electrode, in which 1D nanofibers with porous structure promote the composite electrode to exhibit optimal electrochemical performance.

The cycling performance of the H2@Co$_3$O$_4$ electrode at a current density of 0.1 A g^{-1} was determined (Fig. 3c). The H2@Co$_3$O$_4$ electrode exhibited a large initial discharge capacity of 1368 mAh g^{-1}, which is mainly associated with a series of irreversible reactions during the first discharge process, such as the decomposition of the electrolyte and the formation of SEI films[55]. Even for the 100th cycle, the electrode still preserved a discharge capacity of 916 mAh g^{-1} and a charge capacity of 909 mAh g^{-1}, corresponding to a Coulombic efficiency of 99.2%. Notably, the reversible capacity exceeds the theoretical capacity of 890 mAh g^{-1}, and a rough comparison indicates that the reversible capacity is better than those previously reported[11,13,24,26,39]. However, the theoretical capacity of 890 mAh g^{-1} is predicted by the electrochemical conversion reaction mechanism and calculated by the number of transferred electronics in the reaction[53,56,57]. The excess over the theoretical value most probably arises from interfacial lithium storage in the spaces of the hierarchical pores, which indicates substantial enhancement of Li$^+$ storage capacity and stability for the H2@Co$_3$O$_4$ electrode. Besides, the H1@Co$_3$O$_4$ and H3@Co$_3$O$_4$ electrodes showed acceptable performance with the reversible charge-discharge capacities of 558 and 639 mAh g^{-1} after 100 cycles (Fig. S7), which is about twice of the theoretical value of common commercial graphite (372 mAh g^{-1}). In contrast, the pure Co$_3$O$_4$ exhibited a relative poor cycle performance with the reversible discharge capacity of 293 mAh g^{-1} after 100 cycles. It is worth mentioning that the addition of the carbon substrate can promote the cycling stability of Co$_3$O$_4$. All three H@Co$_3$O$_4$ composite samples have manifested excellent cycling performance compared to the pure Co$_3$O$_4$ electrode. The H2@Co$_3$O$_4$ apparently revealed the best electrochemical performance in all the four electrodes. Moreover, it once again demonstrates that the appropriate content of the carbon substrate in the composite is crucial to lithium storage property. The high electrochemical performance of H2@Co$_3$O$_4$ makes it one of the best known carbon and Co$_3$O$_4$ composite electrodes compared with the other Co$_3$O$_4$–based materials from different methods (Table 1). One thing to point out is that our H2@Co$_3$O$_4$ exhibits better initial discharge capacity and cycling stability at 0.1 A g^{-1}, but the reversible discharge capacity is still lower than that of the result over Co$_3$O$_4$/C sample at the high current density of 2 A g^{-1}, which was synthesized by using oily and expensive surfactant as the source of carbon[40]. Our carbon matrix from human hair is a readily available waste generated in barbershops and hair salons, which is natural, abundant and low cost. The green and facile solvothermal and calcination approach for our crystallized 1D hierarchical porous H2@Co$_3$O$_4$ nanofibers with (220) facets has the potential to large scale production. These observations suggest that the unique H2@Co$_3$O$_4$ fibers architecture and the advanced preparation technique are beneficial for the improvement of Co$_3$O$_4$ anode materials. Therefore, the H2@Co$_3$O$_4$ composites have great potential for Li-ion battery applications.

To further understand the electrochemical kinetics of the $H2@Co_3O_4$ electrode, electrochemical impedance spectroscopy (EIS) measurements were performed after different cycles from 0.1 MHz to 0.01 Hz, in which Z' and Z″ is the real and imaginary part of the impedance, respectively. The measured EIS spectra were analyzed and an equivalent circuit for this cell system is shown in Fig. 3d. In the Nyquist plots, the EIS at high-frequency semicircle corresponds to the resistance of the electrolyte (R_s). The semicircle appearing in the medium frequency range is classically associated with the charge-transfer resistance (R_{ct}) occurring between active materials and liquid electrolyte. The straight line at low-frequency is attributed to the diffusion of lithium ions into electrode materials, or the so-called Warburg impedance (W)[58]. The R_s for the $H2@Co_3O_4$ electrode was 14 Ω after 2 cycles, 2.3 Ω for the 50th cycle and 2.5 Ω at the 100th cycle. This phenomenon demonstrates that the electrode material needs to be activated in the electrolyte at initial cycle, so the value of the second cycle is higher than that in following cycles. When the active materials were fully infiltrated in electrolyte, the value of R_s may increase with increasing cycles. The R_{ct} of the $H2@Co_3O_4$ electrode increased from 190 Ω after 2 cycles to 375 Ω after 50 cycles until to 478 Ω up to the 100th cycle. In general, the Li$^+$ ion conductivity and diffusivity in both liquid and solid phases decrease with long-term continuous charge-discharge since the formation of the SEI membrane on the surfaces of the electrode during the repeated lithiation/delithiation process. The suitable R_{ct} values may be related to the hierarchical porosity of $H2@Co_3O_4$ composite, allowing for the diffusion of electrolyte into the pores more easily and facilitating facial charge transfer at the nanoscale unit/electrolyte interface[41]. For comparison, the EIS plots of the $H1@Co_3O_4$, $H2@Co_3O_4$, $H3@Co_3O_4$ and pure Co_3O_4 electrodes are shown in Figure S8. These plots clearly show that the $H2@Co_3O_4$ electrode reveals the best electrochemical kinetics among that of the $H@Co_3O_4$ and Co_3O_4 electrodes because of the lower ion diffusion resistance in the 1D nanofiber porous structures. The volume inflation/shrinkage or possible exfoliation of the sample during the long charge-discharge process may reduce the embedding of Li$^+$ ion leading to the decline of the specific capacitance and the increase of the impedance. But, the $H2@Co_3O_4$ electrode still exhibits superior cycle stability. Consequently, the superior pore structure may accommodate the volume change of the $H2@Co_3O_4$ composite and the close contact between Co_3O_4 and carbon in the $H2@Co_3O_4$ composite could restraint the exfoliation of the sample during long-term cycling processes. This result indicates that the composite structure of $H2@Co_3O_4$ is beneficial for enhancing the reaction kinetics and the cycling performance of the cells during the charge/discharge process.

Figure 3e exhibits the charge and discharge profiles at different current densities of 0.1, 0.2, 0.5, 1 and 2 A g^{-1}. The discharge capacity of the H2@ Co_3O_4 electrode at different current rate was 1110 (0.1 A g^{-1}), 1054 (0.2 A g^{-1}), 916 (0.5 A g^{-1}), 650 (1 A g^{-1}) and 571 mAh g^{-1} (2 A g^{-1}), respectively. As to the voltage for charge (oxidation) in Fig. 3e, the starting voltage increased with the rising current density from 0.1 to 2 A g^{-1}, which may be due to the increment in polarization voltage at the high current density. It is noteworthy that the separations between the discharge and charge plateaus were enlarged with increasing the current density. This phenomenon may arise from the kinetic effects of the porous electrode material, rendering a higher over-potential[59]. The plateau was still distinguished even at a high current density of 2 A g^{-1} as well as it was at a low current density of 0.1 A g^{11}, indicating that the porous 1D $H2@Co_3O_4$ nanofiber electrode provides superb highways for fast electron transmission and electrolyte ion transport, which may greatly increase the charge rate of the electrode for high-power applications.

To demonstrate the superiority of the unique $H2@Co_3O_4$ electrode, the rate capabilities of the electrode were examined (Fig. 3f) at various current densities from 0.1 to 2 A g^{-1} and then back to 0.1 A g^{-1}. The corresponding discharge capacities were varied accordingly with the discharge rates changing from 1181, to 1060, 890, 683 and 584 mAh g^{-1}. The specific capacity of the $H2@Co_3O_4$ composite could reach 584 mAh g^{-1} even at a high current of 2 A g^{-1}. Notably, the result is apparently superior to recently reported Co_3O_4-based anode materials, such as Co_3O_4/graphene composite showing capacity of 450 mAh g^{-1} at 2.5 A g^{-1} [18], graphene-anchored Co_3O_4 nanoparticle composite delivering capacity of 480 mAh g^{-1} at 500 mA g^{-1} [13], graphene-encapsulated mesoporous Co_3O_4 composite microspheres possessing of capacity of 264 mAh g^{-1} at 2 A g^{-1} [30], peapod-like Co_3O_4/carbon nanocomposites exhibiting capacity of 400 mAh g^{-1} at 1 A g^{-1} [10], Co_3O_4/carbon composite nanowires demonstrating capacity of 358 mAh g^{-1} at 800 mA g^{-1} [60], and graphene-coated Co_3O_4 fibers showing capacity of 295 mAh g^{-1} at 1 A g^{-1} [49]. Remarkably, when the current density returned to 0.1 A g^{-1}, a capacity of 1043 mAh g^{-1} was recovered, indicating the electrode structure remains stable even under the high rate of cycling.

Discussions

We have demonstrated the rational design and fabrication of the hierarchically porous carbon and Co_3O_4 nanocomposites through a facile solvothermal and calcination approach. The content of carbon substrate from hair fiber adjusted by modifying the calcination time of precursor, which not only may reduce the particle-size to form homogeneous nanoparticles but also change the aggregating degree of the particles so as to control the morphology and pore texture of samples. The optimized 1D hierarchical porous $H2@Co_3O_4$ nanofibers with (220) facets served as an anode for LIB applications show a large specific discharge capacity, excellent cycle stability, and high power output characteristic. The advanced preparation technique and high performance suggest that $H2@Co_3O_4$ composite materials have great potential in various energy storage technologies.

Methods

Materials preparation.   The typically straight, middle thickness and black Asian hairs were used for all the experiments, which were collected from a healthy Chinese volunteer in Beihang University. The hair fibers were thoroughly washed with isopropanol and dried at 80 °C. The cleaned fibers were cut into fine debris (~2 mm in length). All the chemicals used in the experiments are analytical grade and were used without further purification. The precursors are synthesized under hydrothermal condition. In a typical synthesis, 2.0 mmol of $Co(CH_3COO)_2 \cdot 4H_2O$ was dissolved in 40 mL of a mixture containing 3.0 mL of ethylene glycol and 37 mL of deionized water. After stirring for 15 min, 0.11 g of urea was added into the above solution. The mixture was stirred for another 30 min. Then 0.2 g of cleaned hair fibers were added into the above solution and immersed for 1 h. The obtained mixture was transferred into a 50 mL Teflon-lined stainless steel autoclave. The autoclave was sealed and maintained at 200 °C for 24 h in an electron oven. After that, the autoclave was cooled naturally to room temperature. The product was collected and washed with deionized water and ethanol for several times by centrifugation, followed by vacuum-drying at 60 °C. After calcinating the collected precursor at 500 °C in air for different time (0.5, 1 and 2 h), the porous $H@Co_3O_4$ composite was obtained, which is accordingly named as $H1@Co_3O_4$, $H2@Co_3O_4$ and $H3@Co_3O_4$, respectively. For comparison, pure Co_3O_4 sample was synthesized under the same synthetic condition as that of $H2@Co_3O_4$ without the hair in the preparation system.

Characterization.   TEM and HRTEM were examined on JEOL JEM-2100F at an acceleration voltage of 200 kV. Powder XRD patterns were determined on the X-ray diffractometor (X-ray 6000) with the 2θ angle region from 10° to 90° at a scan rate of 3° min^{-1}. N_2 adsorption-desorption isotherms were examined at 77 K using a Micromeritics ASAP 2020. Raman spectra were obtained on a microscopic confocal Raman spectrometer (Lab RAM HR800) under a back scattering geometry ($\lambda = 514$ nm). XPS analyses were performed using an Al Kα (150 W) monochromatic X-ray source (ESCALAB 250, Thermo Fisher Scientific, USA). TG analyses were determined at SDTQ600 (TA Instruments, USA) under an air atmosphere at a heating rate of 10 °C min^{-1} from room temperature to 800 °C. CV was performed by using CHI1040C electrochemical work station between 0.01 and 3.00 V at a scan rate of 0.2 mV s^{-1}. The galvanostatic charging/discharging test was conducted by using coin cells (CR2032) at room temperature on a multi-channel battery testing system (LAND CT2001A) with a cutoff voltage of 3.00–0.01 V vs Li^+/Li. Working electrodes were prepared by mixing 80 wt.% the Co_3O_4 or $H@Co_3O_4$ material, 10 wt.% acetylene black (Super-P), and 10 wt.% polyvinylidenefluoride (PVDF) binder dissolved in N-methyl-2-pyrrolidinone (NMP). 1.0 M $LiPF_6$ in mixed ethylene carbonate (EC) and diethyl carbonate (DEC) (EC: DEC = 1:1 by volume) was used as the electrolyte in the system. EIS measurements were conducted for the working electrode in a frequency range of 0.1 MHz to 0.01 Hz.

References

1. Wang, H. *et al.* Mn_3O_4-graphene hybrid as a high-capacity anode material for lithium ion batteries. *J. Am. Chem. Soc.* **132,** 13978–13980 (2010).
2. Zhao, L., Hu, Y. S., Li, H., Wang, Z. & Chen, L. Porous $Li_4Ti_5O_{12}$ coated with N-doped carbon from ionic liquids for Li-ion batteries. *Adv. Mater.* **23,** 1385–1388 (2011).
3. Lai, X., Halpert, J. E. & Wang, D. Recent advances in micro-/nano-structured hollow spheres for energy applications: From simple to complex systems. *Energy Environ. Sci.* **5,** 5604–5618 (2012).
4. Xiao, Y., Hu, C. & Cao, M. Facile microstructure control of mesoporous $Co_{1.29}Ni_{1.71}O_4$ and the effect of the microstructure on lithium-storage performance. *Chem. Eur. J.* **19,** 10193–10200 (2013).
5. Kang, B. & Ceder, G. Battery materials for ultrafast charging and discharging. *Nature* **458,** 190–193 (2009).
6. Armand, M. & Tarascon, J. M. Building better batteries. *Nature* **451,** 652–657 (2008).
7. Qie, L. *et al.* Nitrogen-doped porous carbon nanofiber webs as anodes for lithium ion batteries with a superhigh capacity and rrate capability. *Adv. Mater.* **24,** 2047–2050 (2012).
8. Suo, L., Hu, Y. S., Li, H., Armand, M. & Chen, L. A new class of solvent-in-salt electrolyte for high-energy rechargeable metallic lithium batteries. *Nat. Commun.* **4,** 1481 (2013).
9. Wang, F. *et al.* Tracking lithium transport and electrochemical reactions in nanoparticles. *Nat. Commun.* **3,** 1201–1208 (2012).
10. Wang, Y. *et al.* Designed functional systems from peapod-like Co@carbon to Co_3O_4@carbon nanocomposites. *ACS Nano* **4,** 4753–4761 (2010).
11. Wang, X. *et al.* Synthesis and lithium storage properties of Co_3O_4 nanosheet-assembled multishelled hollow spheres. *Adv. Funct. Mater.* **20,** 1680–1686 (2010).
12. Wang, Y., Xia, H., Lu, L. & Lin, J. Excellent performance in lithium-ion battery anodes: Rational synthesis of $Co(CO_3)_{0.5}(OH)_{0.11}H_2O$ nanobelt array and its conversion into mesoporous and single-crystal Co_3O_4. *ACS Nano* **4,** 1425–1432 (2010).
13. Wu, Z. S. *et al.* Graphene anchored with Co_3O_4 nanoparticles as anode of lithium ion batteries with enhanced reversible capacity and cyclic Performance. *ACS Nano* **4,** 3187–3194 (2010).
14. Liu, D. *et al.* Co_3O_4 nanocages with highly exposed {110} facets for high-performance lithium storage. *Sci. Rep.* **3,** 2543–2548 (2013).
15. Zhu, J. *et al.* Cobalt oxide nanowall arrays on reduced graphene oxide sheets with controlled phase, grain size, and porosity for Li-ion battery electrodes. *J. Phys. Chem. C* **115,** 8400–8406 (2011).
16. Sun, H. *et al.* Mesoporous Co_3O_4 nanosheets-3D graphene networks hybrid materials for high-performance lithium ion batteries. *Electrochimica Acta* **118,** 1–9 (2014).
17. Nethravathi, C. *et al.* Cobalt hydroxide/oxide hexagonal ring-graphene hybrids through chemical etching of metal hydroxide platelets by graphene oxide: Energy storage applications. *ACS Nano* **8,** 2755–2765 (2014).
18. Xu, M. *et al.* Co_3O_4-carbon nanotube heterostructures with bead-on-string architecture for enhanced lithium storage performance. *Nanoscale* **5,** 8067–8072 (2013).
19. Zhou, G., Li, L., Zhang, Q., Li, N. & Li, F. Octahedral Co_3O_4 particles threaded by carbon nanotube arrays as integrated structure anodes for lithium ion batteries. *PCCP* **15,** 5582–5587 (2013).

20. Venugopal, N., Lee, D.-J., Lee, Y. J. & Sun, Y.-K. Self-assembled hollow mesoporous Co_3O_4 hybrid architectures: a facile synthesis and application in Li-ion batteries. *J. Mater. Chem. A* **1,** 13164–13170 (2013).

21. Hao, F., Zhang, Z. & Yin, L. Co_3O_4/carbon aerogel hybrids as anode materials for lithium-ion batteries with enhanced electrochemical properties. *ACS Appl. Mater. Interf.* **5,** 8337–8344 (2013).

22. Wang, Y. *et al.* Onion-like carbon matrix supported Co_3O_4 nanocomposites: a highly reversible anode material for lithium ion batteries with excellent cycling stability. *J. Mater. Chem. A* **1,** 5212–5216 (2013).

23. Jayaprakash, N., Jones, W. D., Moganty, S. S. & Archer, L. A. Composite lithium battery anodes based on carbon@Co_3O_4 nanostructures: Synthesis and characterization. *J. Power Sources* **200,** 53–58 (2012).

24. Li, Y., Tan, B. & Wu, Y. Mesoporous Co_3O_4 nanowire arrays for lithium ion batteries with high capacity and rate capability. *Nano Lett.* **8,** 265–270 (2007).

25. Feng, X. Y., Shen, C., Yu, Y., Wei, S. Q. & Chen, C. H. Synthesis and electrochemical properties of sticktight-like and nanosheet Co_3O_4 particles. *J. Power Sources* **230,** 59–65 (2013).

26. Lou, X. W., Deng, D., Lee, J. Y., Feng, J. & Archer, L. A. Self-supported formation of needlelike Co_3O_4 nanotubes and their application as lithium-ion battery electrodes. *Adv. Mater.* **20,** 258–262 (2008).

27. Wang, X. *et al.* Synthesis of single-crystalline Co_3O_4 octahedral cages with tunable surface aperture and their lithium storage properties. *J. Phys. Chem. C* **113,** 15553–15558 (2009).

28. Li, L., Seng, K. H., Chen, Z., Guo, Z. & Liu, H. K. Self-assembly of hierarchical star-like Co_3O_4 micro/nanostructures and their application in lithium ion batteries. *Nanoscale* **5,** 1922–1928 (2013).

29. Wang, F. *et al.* Solid state coalescence growth and electrochemical performance of plate-like Co_3O_4 mesocrystals as anode materials for lithium-ion batteries. *J. Power Sources* **235,** 67–73 (2013).

30. Yang, X. *et al.* Tailored graphene-encapsulated mesoporous Co_3O_4 composite microspheres for high-performance lithium ion batteries. *J. Mater. Chem.* **22,** 17278–17283 (2012).

31. Zhang, H. *et al.* From cobalt nitrate carbonate hydroxide hydrate nanowires to porous Co_3O_4 nanorods for high performance lithium-ion battery electrodes. *Nanotechnology* **19,** 1–5 (2008).

32. Huang, H. *et al.* Nanocrystal-constructed mesoporous single-crystalline Co_3O_4 nanobelts with superior rate capability for advanced lithium-ion batteries. *ACS Appl. Mater. Interf.* **4,** 5974–5980 (2012).

33. Favors, Z. *et al.* Stable cycling of SiO_2 nanotubes as high-performance anodes for lithium-ion batteries. *Sci. Rep.* **4,** 4605–4611 (2014).

34. Wang, B. *et al.* Mesoporous CNT@TiO_2-C nanocable with extremely durable high rate capability for lithium-ion battery anodes. *Sci. Rep.* **4,** 3729–3735 (2014).

35. Mai, L. *et al.* Electrospun ultralong hierarchical vanadium oxide nanowires with high performance for lithium ion batteries. *Nano Lett.* **10,** 4750–4755 (2010).

36. Su, D., Ford, M. & Wang, G. Mesoporous NiO crystals with dominantly exposed {110} reactive facets for ultrafast lithium storage. *Sci. Rep.* **2,** 924–930 (2012).

37. Wei, G. Z. *et al.* Crystal habit-tuned nanoplate material of $Li[Li_{1/3-2x/3}Ni_xMn_{2/3-x/3}]O_2$ for high-rate performance lithium-ion batteries. *Adv. Mater.* **22,** 4364–4367 (2010).

38. Qian, W. *et al.* Human hair-derived carbon flakes for electrochemical supercapacitors. *Energy Environ. Sci.* **7,** 379–386 (2014).

39. Li, W. Y., Xu, L. N. & Chen, J. Co_3O_4 nanomaterials in lithium-ion batteries and gas sensors. *Adv. Funct. Mater.* **15,** 851–857 (2005).

40. Sun, J., Liu, H., Chen, X., Evans, D. G. & Yang, W. An oil droplet template method for the synthesis of hierarchical structured Co_3O_4/C anodes for Li-ion batteries. *Nanoscale* **5,** 7564–7571 (2013).

41. Xiao, Y., Hu, C. & Cao, M. High lithium storage capacity and rate capability achieved by mesoporous Co_3O_4 hierarchical nanobundles. *J. Power Sources* **247,** 49–56 (2014).

42. Zhang, G. & Lou, X. W. General solution growth of mesoporous $NiCo_2O_4$ nanosheets on various conductive substrates as high-performance electrodes for supercapacitors. *Adv. Mater.* **25,** 976–979 (2013).

43. Dong, X.-C. *et al.* 3D Graphene–cobalt oxide electrode for high-performance supercapacitor and enzymeless glucose detection. *ACS Nano* **6,** 3206–3213 (2012).

44. Zhang, L. *et al.* Novel three-dimensional Co_3O_4 dendritic superstructures: hydrothermal synthesis, formation mechanism and magnetic properties. *CrystEngComm* **15,** 1389–1396 (2013).

45. Li, B. *et al.* Co_3O_4@graphene composites as anode materials for high-performance lithium ion batteries. *Inorg. Chem.* **50,** 1628–1632 (2011).

46. Zhou, G.-M. *et al.* Oxygen bridges between NiO nanosheets and graphene for improvement of lithium storage, *ACS Nano* **6,** 3214–3223 (2012).

47. Jadhav, H. S., Rai, A. K., Lee, J. Y., Kim, J. & Park, C.-J. Enhanced electrochemical performance of flower-like Co_3O_4 as an anode material for high performance lithium-ion batteries. *Electrochimica Acta* **146,** 270–277 (2014).

48. Xiong, S., Chen, J. S., Lou, X. W. & Zeng, H. C. Mesoporous Co_3O_4 and CoO@C topotactically transformed from chrysanthemum-like $Co(CO_3)_{0.5}(OH)\cdot0.11H_2O$ and their lithium-storage properties. *Adv. Funct. Mater.* **22,** 861–871 (2012).

49. Yang, X. *et al.* Electric papers of graphene-coated Co_3O_4 fibers for high-performance lithium ion batteries. *ACS Appl. Mater. Interf.* **5,** 997–1002 (2013).

50. Lian, P. *et al.* Enhanced cycling performance of Fe_3O_4-graphene nanocomposite as an anode material for lithium-ion batteries. *Electrochimica Acta* **56,** 834–840 (2010).

51. Fan, Y. *et al.* Synthesis of foam-like freestanding Co_3O_4 nanosheets with enhanced electrochemical activities. *Chem. Commun.* **47,** 3469–3471 (2011).

52. Wang, L. *et al.* Nanorod-assembled Co_3O_4 hexapods with enhanced electrochemical performance for lithium-ion batteries. *J. Mater. Chem.* **22,** 23541–23546 (2012).

53. Yao, X. *et al.* Co_3O_4 nanowires as high capacity anode materials for lithium ion batteries. *J. Alloys Compd.* **521,** 95–100 (2012).

54. Sun, H. *et al.* High-rate lithiation-induced reactivation of mesoporous hollow spheres for long-lived lithium-ion batteries. *Nat. Commun.* **5,** 5526–5533 (2014).

55. Poizot, P., Laruelle, S., Grugeon, S., Dupont, L. & Tarascon, J. M. Searching for new anode materials for the Li-ion technology: time to deviate from the usual path. *J. Power Sources* **97-98,** 235–239 (2001).

56. Zhan, F., Geng, B. & Guo, Y. Porous Co_3O_4 nanosheets with extraordinarily high discharge capacity for lithium batteries. *Chem. Eur. J.* **15,** 6169–6174 (2009).

57. Wang, C., Wang, D., Wang, Q. & Wang, L. Fabrication of three-dimensional porous structured Co_3O_4 and its application in lithium-ion batteries. *Electrochimica Acta* **55,** 6420–6425 (2010).

58. Yang, C. *et al.* Superlow load of nanosized MnO on a porous carbon matrix from wood fibre with superior lithium ion storage performance. *J. Mater. Chem. A* **2,** 19975–19982 (2014).

59. Wang, R. *et al.* Free-standing and binder-free lithium-ion electrodes based on robust layered assembly of graphene and Co_3O_4 nanosheets. *Nanoscale* **5,** 6960–6967 (2013).

60. Zhang, P., Guo, Z. P., Huang, Y., Jia, D. & Liu, H. K. Synthesis of Co_3O_4/carbon composite nanowires and their electrochemical properties. *J. Power Sources* **196,** 6987–6991 (2011).

Acknowledgement

Author Contributions

Q.-M.G. planned and supervised the project; Y.-L.T. and Q.-M.G. designed and performed experiments; Y.-L.T., C.-X.Y., K.Y., W.-Q.T. and L.-H.Z. carried out the electrochemical property tests. Q.-M.G. and Y.-L.T. analyzed data and wrote the manuscript; and all authors discussed the results and commented on the manuscript.

Additional Information

Supplementary information accompanies this paper at http://www.nature.com/srep

Competing financial interests: The authors declare no competing financial interests.

How to cite this article: Tan, Y. *et al.* One-dimensional porous nanofibers of Co3O4 on the carbon matrix from human hair with superior lithium ion storage performance. *Sci. Rep.* **5**, 12382; doi: 10.1038/srep12382 (2015).